*J. Fluid Mech.* (2005), *vol.* 527, *pp.* 1–25.  
DOI: 10.1017/S0022112004002770 Printed in the United Kingdom

# Transition induced by free-stream turbulence

By J. H. M. FRANSSON[1], M. MATSUBARA[2,1] AND P. H. ALFREDSSON[1]

[1]KTH Mechanics, SE-100 44 Stockholm, Sweden

[2]Department of Mechanical Systems Engineering, Shinshu University, Nagano, Japan

(Received 8 December 2003 and in revised form 30 July 2004)

Free-stream turbulence (FST) is perhaps the most important source inducing by-pass transition in boundary layer flows. The present study describes the initial energy growth of streamwise-oriented disturbances in the boundary layer originating from the presence of FST with intensities between 1.4% and 6.7%, but the study is mainly focused on the modelling of the transition zone. For this study three passive and one active turbulence-generating grids were used. The active grid was used in order to vary the turbulence intensity ($Tu$) without changing the setup in the test section. It is shown that the initial disturbance energy in the boundary layer is proportional to $Tu^2$. The experiments also show that the energy grows in linear proportion to the Reynolds number based on the downstream distance. Furthermore the transitional Reynolds number is shown to be inversely proportional to $Tu^2$ for the whole range of $Tu$ studied. The intermittency in the transitional zone was determined and it was shown that the intermittency function has a universal shape if the downstream distance is scaled with the length of the transition zone. The Reynolds number based on this transition zone length was found to increase linearly with the transition Reynolds number; however it was also noted that this non-dimensional length has a minimum value. With these results we were able to formulate an expression for the spot production rate which has a better physical base than previous models.

## 1. Introduction

It is known that a boundary layer subject to free-stream turbulence (FST) develops unsteady streaky structures with high and low streamwise velocities (for reviews see Kendall 1998; Westin 1997). This leads to large-amplitude, low-frequency fluctuations inside the laminar boundary layer when measured by a stationary hot wire. Flow visualization photos show the presence of streaky structures (see e.g. Matsubara & Alfredsson 2001), and it is apparent that the FST gives rise to longitudinal structures in the flow with a relatively well-defined spanwise scale. In flow visualization experiments the streaks have been seen to develop a streamwise waviness, which may break down into turbulent spots. These spots subsequently grow until the boundary layer is fully turbulent.

Over the past two decades several experimental studies have investigated disturbance growth and transition under the influence of FST. Kendall (1985) observed low-frequency fluctuations in the boundary layer that grow in linear proportion to $x^{1/2}$ (i.e. proportional to the laminar boundary layer thickness, $\delta$). He also observed the occurrence of elongated streamwise structures with narrow spanwise scales. Westin *et al.* (1994) made detailed measurements of a laminar boundary layer disturbed by

FST and showed among other things that the Blasius profile was only slightly modified, despite $u_{\rm rms}$ levels of about 10% inside the boundary layer before breakdown. They also confirmed that the growth of $u_{\rm rms}$ was proportional to $x^{1/2}$. It has been possible to put these results into the theoretical framework of so-called algebraic or transient growth, see for instance Andersson, Berggren & Henningson (1999) or Luchini (2000). This theory shows that streamwise elongated structures may grow in amplitude as $x^{1/2}$ even at low Reynolds numbers and comparisons between the theoretical amplitude variation and the measured distributions of $u_{\rm rms}$ show excellent agreement. Transient growth theory is linear, which is why a comparison with FST-induced transition only should be adequate until secondary instabilities on the streaks set in and nonlinear effects become significant. Fransson *et al.* (2004) investigated stationary and steady streaks, generated by means of an array of roughness elements in the spanwise direction. They showed that transient growth theory is in good agreement with the experimentally observed steady streaks throughout the entire transient growth region (i.e. both through growth and decay).

The spanwise scale of the streaks decreases with increasing turbulence intensity ($Tu$) and for the Blasius boundary layer this scale seems to adapt to the boundary layer thickness after an initial mismatch (see Matsubara & Alfredsson 2001). Fransson & Alfredsson (2003) carried out FST experiments on an asymptotic suction boundary layer and showed that with a reduction of the boundary layer thickness by a factor of two the spanwise scale of the streaks was maintained, giving rise to a spanwise widening of the streaky structure relative to the boundary layer thickness, in contrast to the results by Matsubara & Alfredsson. Furthermore, they conclude that the most amplified spanwise scale predicted by algebraic growth theory is approached for increasing $Tu$. The results by Yoshioka, Fransson & Alfredsson (2004) in boundary layers with suction indicate that the observed spanwise scale is a complex result of the initial growth near the leading edge in the receptivity region, the FST scales and the downstream development of the boundary layer.

There have also recently been some direct numerical simulations of the FST transition process (see Jacobs & Durbin 2001; Brandt, Schlatter & Henningson 2004). In these cases the leading-edge region is not simulated; instead the simulation is started at some downstream position with a turbulent free stream. The simulations also show the generation of longitudinal streaks and the breakdown to turbulent spots. Brandt *et al.* showed that both sinuous and varicose secondary instabilities of the streaks may be a precursor to the formation of turbulent spots.

In experiments there are two essential factors that determine the response to the forcing (the so-called receptivity process) by the FST. First, the geometry of the leading edge plays a role. A symmetric leading edge gives rise to a pressure suction peak, which results in a local negative pressure gradient followed by a positive one. This is the reason for using an asymmetric leading-edge design (see e.g. Klingmann *et al.* 1993; Fransson & Alfredsson 2003; Fransson 2004), which is also necessary to obtain good agreement with linear stability theory. Secondly, the nature of the disturbances that affect the boundary layer is important. In case of FST disturbances these are described by the characteristic scales of the turbulence and the energy-frequency spectra of the various components. Of course there may also be other types of forcing which are unwanted, such as vibrations or noise, and experimental results may therefore differ from facility to facility.

In order to further understand the transition process, results from theory, simulations and experiments need to be studied and compared. Simulations are quite time consuming and not suitable for parameter variations; however they can provide

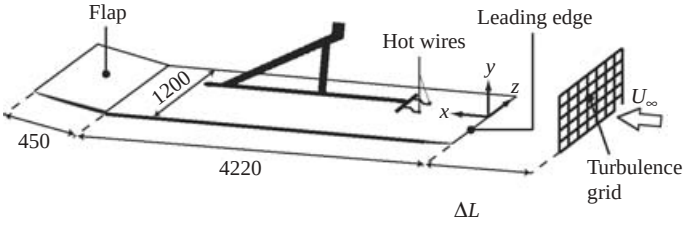


FIGURE 1. Schematic view of the experimental setup (dimensions in mm).

details of the flow which are not available in experiments. Another drawback is that the simulations so far have not covered the leading-edge region which probably has an influence on the subsequent disturbance development. On the other hand various experiments give quantitatively different results for the transition position which may be due to differences in the experimental conditions. One such factor that may influence the transition is the effect of different FST scales on the receptivity at the leading edge. It would therefore be advantageous to perform experiments with small variations of the FST scales, in order to reduce such an influence on the experimental results. However, to design turbulence-generating grids that generate different *Tu* levels and at the same time have the same turbulence scales (both regarding the turbulence decay and the energy-containing scales) is a demanding task, and such studies may therefore be more suitable for direct numerical simulations where such requirements may be controlled easily (see e.g. Brandt *et al.* 2004). The major part of the results in this paper is from an active grid which allows an easy change of the *Tu* level but for which, however, the problem of different generated scales remains.

The present paper starts with a brief introduction of the experimental setup followed by a thorough description of the turbulence-generating grids. Thereafter, a standard intermittency estimation technique with an improvement on the threshold determination is described. Finally, the results are shown and discussed in terms of modelling and transition prediction.

## 2. Experimental setup

The experiments were performed in the MTL (Minimum Turbulence Level or Mårten T. Landahl named after its late initiator) wind-tunnel at KTH where a 4.2 m long test plate was mounted horizontally in the test section. Over the past decade several studies on different aspects of FST-induced by-pass transition have been reported from the KTH Mechanics group with roughly the same experimental setup (refer to Matsubara & Alfredsson 2001 for details of the experimental setup). Briefly, the test section is 7 m long with a cross-sectional area of $1.2 \times 0.8\,\mathrm{m}^2$, and is equipped with a five-degree traversing mechanism (namely, $(x, y, z)$-directions plus two angle movements); see figure 1 for a schematic view of the flat plate setup. The flat plate has an asymmetric leading edge which together with the adjustable trailing flap has been designed in order to obtain a near zero pressure gradient in the leading edge region also.

Recently, the flow quality of the MTL wind tunnel was re-confirmed after 10 years in operation. An important aspect of wind-tunnel flow quality is the level of turbulence intensity in the test section, but despite this, there is no standard procedure for selecting the frequency range to be used in specifying tunnel turbulence levels. In transition experiments this issue becomes even more delicate since it is desirable that all disturbances are controlled by the experimentalist. Here, we therefore provide both

| Grid | Bar geometry | $M$ (mm) | $d_p$ (mm) | $S_g$ | $Tu$ (%) | $\Delta L$ |
|---|---|---|---|---|---|---|
| A | circular | 36 | 6 | 0.31 | 2.2–2.5 | 1600 |
| B | circular | 23 | 3.5 | 0.28 | 1.5 | 1600 |
| E | square | 50 | 10 | 0.36 | 5.3–6.7 | 1000 |
| G | circular | 50 | 5 | 0.19 | 1.4–5.3 | 1000–1600 |

TABLE 1. Passive (A, B, and E) and active (G) grid characteristics. See text for definitions.

the high-pass filtered and the unfiltered data of the turbulence intensities reported in Lindgren (2002), in which the cut-off frequency ($f_c = U_\infty/\lambda_c$) was chosen such that all disturbances with wavelengths fitting in the test section cross-section were to be conserved. As reported in Lindgren the cut-off wavelength ($\lambda_c$) was chosen to be 2.0 m, i.e. the sum of the two test section side lengths, in order to allow for some margin. At 25 m s$^{-1}$ the high-pass filtered and the total unfiltered streamwise turbulence intensities are less than 0.025% and 0.080%, respectively. Both the cross-flow turbulence intensities are less than 0.035% and 0.040% for the high-pass filtered and unfiltered intensities, respectively.

Furthermore, the total pressure and temperature variations are less than $\pm 0.06\%$ and $\pm 0.05\,^\circ$C, respectively. For full details of the tunnel the interested reader is refered to Lindgren (2002). The data in the present experiments were collected with hot-wire anemometry of both single- and X-probe type. The single probe was calibrated in the wind tunnel against a Prandtl tube and then a modified King's law (cf. Johansson & Alfredsson 1982), taking into account the natural convection, was used for curve fitting. For the X-probe an angle calibration was carried out and a two-dimensional fifth-order polynomial was fitted to the calibration data, giving $U$ and $V$ as functions of the obtained voltage pair.

## 3. Turbulence-generating grids

Free-stream turbulence is usually generated with the use of grids made of bars with circular or square cross-section. The scale and intensity of the FST is related to the geometry of the bars and the grid, i.e. the mesh width ($M$), bar width ($d_p$) and the corresponding geometric solidity ($S_g$), as well as the Reynolds number. The turbulence level usually increases with the solidity, but also depends on the flow velocity and hence the Reynolds number of the grid. An alternative, which makes it possible to generate different FST intensities without changing the set-up in the test section, is to use an active grid with injection of secondary flow. An example of such an active grid was studied by Gad-El-Hak & Corrsin (1974) where both coflow and counterflow injection were compared with the zero injection case (however in their case the 'grid' only consisted of horizontal pipes).

In the present study the FST was generated by four different grids, three passive grids (A, B, E), and one active grid G, mounted at different positions ($\Delta L = 1000$–$1600$ mm) upstream of the leading edge. Grid G is active in the sense that it ejects secondary flow in the form of jets directed upstream, i.e. counterflow injection. The free-stream velocity ($U_\infty$) was varied in the range 2–14 m s$^{-1}$ and a variation of $\Delta L$ provided streamwise turbulence levels ($Tu = u_{\rm rms}/U_\infty$) in the range 1.4% to 6.7% at the leading edge of the plate. For all grids the transverse turbulence level ($Tv = v_{\rm rms}/U_\infty$) was slightly lower at the leading edge. In table 1 the main characteristics of all four grids are summarized.

### 3.1. *Turbulence scales*

Downstream of the grid the turbulence decays and the typical power-law decay can be described according to

$$Tu = \frac{u_{\mathrm{rms}}}{U_\infty} = C(x - x_0)^{-b}, \tag{3.1}$$

where $x_0$ is a virtual origin of the grid, the exponent $b$ gives the decay rate and the constant $C$ gives the level for a particular grid and $Re$. A simple analysis (see e.g. Tennekes & Lumley 1997) gives $b = 0.5$. Recent works, both experiments and direct numerical simulations, have shown the value to be closer to $b = 0.6$ (see e.g. Oberlack 2002) for isotropic turbulence.

In addition to the turbulence intensities generated by the grid, the FST scales are of interest, and can be obtained from either spatial correlation measurements using two hot wires or from the autocorrelation calculated from the time signal measured by a single hot wire. Here we describe how to obtain these values from the autocorrelation, but the definitions and methods are applicable to the spatial correlations as well. The autocorrelation function of the streamwise fluctuating velocity and the integral (macro) time scale ($\Lambda$) are defined as

$$R_{uu}(t^*) \equiv \frac{\overline{u(t)u(t')}}{u_{\mathrm{rms}}^2} \tag{3.2}$$

and

$$\Lambda = \int_0^\infty R_{uu}(t^*)\,\mathrm{d}t^* \tag{3.3}$$

respectively, where $t^* = t' - t$ and overbar denotes time averaging. The Taylor microscale ($\tau_t$) may be viewed as the smallest energetic time scale and can be estimated directly from the curvature of the autocorrelation function at $t^* = 0$, but can also be expressed as

$$\tau_t^2 \equiv 2\frac{\overline{u^2}}{\overline{(\partial u/\partial t)^2}}. \tag{3.4}$$

This expression is derived through Taylor series expansion of the correlation coefficient function (see e.g. Tennekes & Lumley 1997) and was used by Hallbäck, Groth & Johansson (1989) to calculate a measured (denoted by subscript $m$) time scale by computing

$$\tau_{tm}^2 = 2\frac{\overline{u^2}}{\overline{(\Delta u/\Delta t)^2}} \tag{3.5}$$

for various values of $\Delta t$. Thereafter the expression

$$\left(\frac{\tau_{tm}}{\tau_t}\right)^2 = 1 + \beta\frac{\Delta t}{\tau_t} \tag{3.6}$$

is fitted to data in the region $0.1 < \Delta t/\tau_t < 0.35$, which makes it possible to accurately determine $\tau_t$. Hallbäck *et al.* noted that the lower limit is necessary since at small $\Delta t$ the effect of electrical noise and insufficient resolution in the AD-converter give a too low value of the microscale.

From the decay of the FST (3.1) the dissipation rate can be determined. For isotropic turbulence it is possible to find a relation between the Taylor scale and the

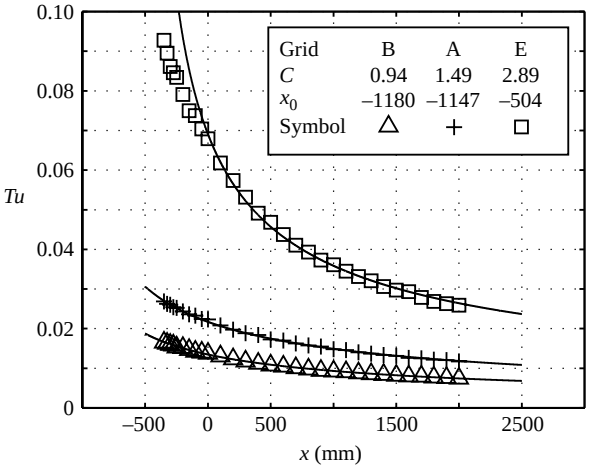


FIGURE 2. Turbulence decay for grids A, B and E. The curves are fitted to experimental data according to (3.1) with $b = 0.60$ (for grid E only data for which $x > 0$ has been used). Grids A and E: $U_\infty = 8\,\mathrm{m\,s^{-1}}$, grid B: $U_\infty = 12\,\mathrm{m\,s^{-1}}$.

dissipation rate (see e.g. Tennekes & Lumley 1997) which can be expressed as

$$\tau_{\mathrm{x,isotropic}} = \left[\frac{5\nu(x - x_0)}{bU_\infty}\right]^{1/2}. \tag{3.7}$$

It should also be noted that for isotropic turbulence there is a relation between the Taylor scales obtained from e.g. $R_{uu}(x^*)$ and $R_{uu}(z^*)$ which is $\tau_x = \sqrt{2}\tau_z$. Similarly, the Taylor scales obtained from the autocorrelation of $u$ and $v$ are related in the same way.

### 3.2. *Passive grids*

Transition data from three different passive grids were used in this work. These are the same grids as used in e.g. Matsubara & Alfredsson (2001). Grids A and B are commercially available and made of steel wires with circular cross-section. These grids have a slightly larger size than the test section and are pressed into position at the junction of the contraction and the test section. Grid E, on the other hand, was specially built to fit the test section and is a monoplane grid constructed out of square cylindrical bars with a cross section of $10\,\mathrm{mm}^2$ and is always positioned 600 mm downstream of the start of the test section.

The variation of the streamwise turbulence intensity along the test section for these grids is shown in figure 2 for a free-stream velocity of $8\,\mathrm{m\,s^{-1}}$ for grids A and E and $12\,\mathrm{m\,s^{-1}}$ for grid B. The lines shown in the graph are fitted using (3.1) with $b = 0.6$. For grid E only data points for which $x > 0$ are used, corresponding to distances from the grid larger than $20M$.

The Taylor scales of the turbulence behind these grids were determined both from autocorrelation X-probe measurements ($\tau_t(u)$, $\tau_t(v)$) and spatial correlations using two single hot wires ($\tau_z(u)$). The results obtained at the leading edge are shown in table 2. First one may note that for all grids $Tv < Tu$. Secondly we see that the two completely different methods to determine the transverse Taylor scale ($\tau_t(v)$ and $\tau_z(u)$)

| Grid | $x/M$ | $Tu$ (%) | $Tv$ (%) | $\tau_x(u)$ (mm) | $\tau_x(v)$ (mm) | $\tau_z(u)$ (mm) |
|---|---|---|---|---|---|---|
| A | 44 | 2.2 | 1.9 | 8.7 | 5.0 | 5.2 |
| B | 70 | 1.5 | 1.3 | 7.0 | 4.5 | 5.0 |
| E | 20 | 6.1 | 5.0 | – | – | 4.1 |

TABLE 2. Turbulence characteristics of grids A, B, and E measured at the leading edge of the plate at $U_\infty = 8\,\mathrm{m\,s^{-1}}$.

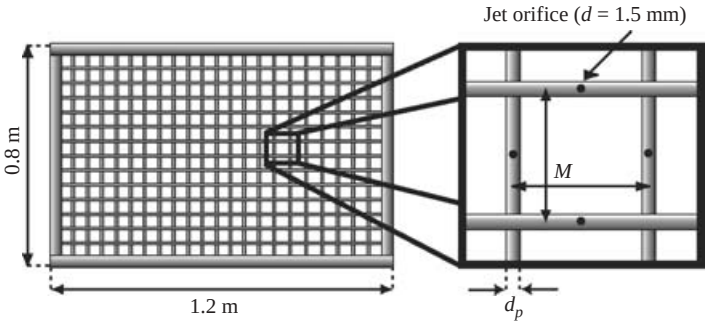


FIGURE 3. Active grid (G) with main dimensions.

give similar results for grids A and B.† Finally we see that the longitudinal Taylor scale is approximately a factor of 1.5 larger than the transverse scale. This can be compared to the theoretical factor for isotropic turbulence which is $\sqrt{2}$.

### 3.3. *Active grid*

The active grid consists of a rectangular frame with dimension $1.2 \times 0.8\,\mathrm{m}^2$ (width $\times$ height, identical with the dimension of the MTL test section). Each side of this frame is separated from the others and consists of a brass pipe with an outer diameter of 15 mm (wall thickness = 1 mm) and has two inlets for secondary air. A total of 33 brass pipes, 20 vertically and 13 horizontally, were soldered to the frame. These pipes have a diameter of 5 mm (wall thickness 0.9 mm) and are located to give a mesh width $M = 50$ mm, which corresponds to a geometrical solidity ($S_g$) of 0.19. The jet orifices have a diameter of 1.5 mm and are directed upstream in the present setup. The orifices are concentrated in the middle section of the grid and there is a total of 254 (12 horizontally $\times$ 12 and 11 vertically $\times$ 10, cf. figure 3 for an illustration of the grid geometry). A fine-meshed screen (mosquito type) was positioned on the downstream side of the frame in order to improve the homogeneity of the flow.

The secondary flow is supplied to the grid through flexible rubber tubing connected to the inlets at the frame. The air is driven by a modified vacuum cleaner (1 kW) and the injection rate was regulated by a transformer. In the results sections of the present study many different injection rates were used, but in this section results from three different rates (none, moderate and high) will be shown. These are denoted as G0, G1 and G2, which correspond to an upstream injection of $(0, 5, 10)\,1\,\mathrm{s^{-1}}$ or an individual jet velocity of (0, 11, 21) $\mathrm{m\,s^{-1}}$, respectively. All the characteristics of the grid presented in this section were obtained at a free-stream velocity of $5\,\mathrm{m\,s^{-1}}$

† The time scales were transformed to streamwise length scales through Taylor's hypothesis (frozen turbulence approximation), e.g. $\tau_x = U_\infty \tau_t$.

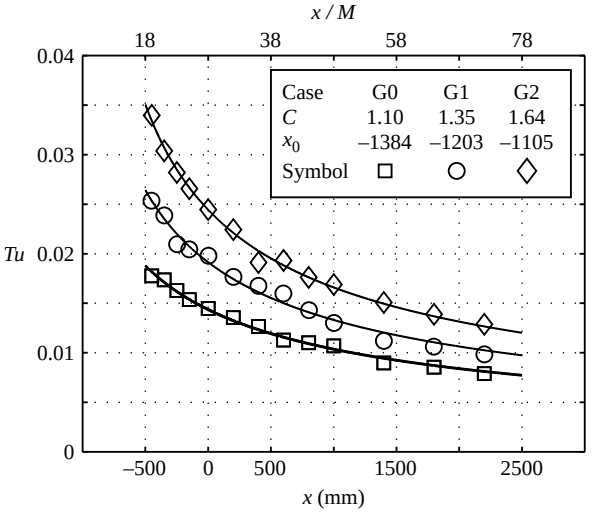


FIGURE 4. Turbulence decay for different injection rates. The curves are fitted to experimental data according to (3.1) with $b = 0.60$.

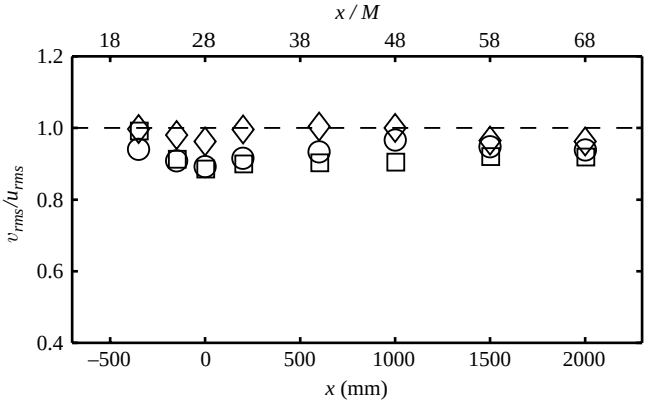


FIGURE 5. The isotropy measure $v_{\rm rms}/u_{\rm rms}$ as a function of the downstream distance. □, G0; ○, G1; ◇, G2.

corresponding to a maximum injection flow rate of approximately 0.5% through the active part of the grid. In the transition experiments the maximum injection rate is obtained at $U_\infty = 2\,\mathrm{m\ s^{-1}}$, and corresponds to less than 1.5%.

### 3.3.1. *Turbulence decay*

In figure 4 the downstream development of $Tu$ for the three injection cases G0, G1 and G2 is shown. The grid distance upstream of the leading edge was fixed here at $x = -1400\,\mathrm{mm}$ corresponding to $28M$ from the leading edge of the plate. The curve fits are done using (3.1) with $b = 0.6$. This figure clearly shows the increase of $Tu$ with increasing injection rate for all downstream positions from the grid.

In figure 5 the isotropy measure $v_{\rm rms}/u_{\rm rms}$ behind the active grid is plotted as a function of the downstream distance for different injection rates. The figure shows a nearly isotropic turbulence for all three cases at $x = -400\,\mathrm{mm}$, which is in agreement with the rule of thumb that $20M$ is needed to establish nearly isotropic turbulence behind a grid. All three cases have an isotropy measure above 0.9 and the highest

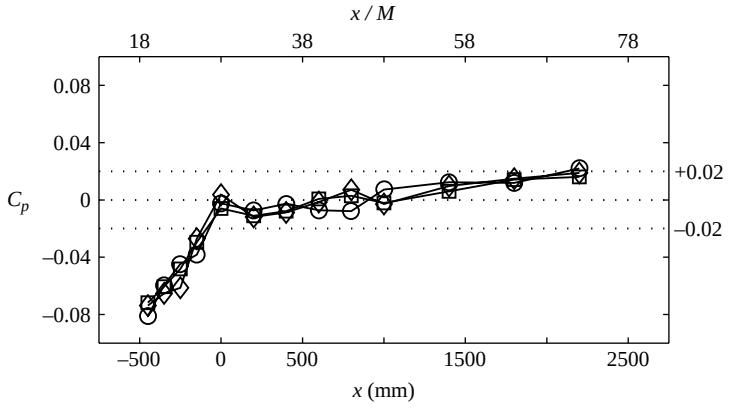


FIGURE 6. Pressure distribution vs the downstream distance for different injection rates (see figure 5 for symbols).

*Tu* achieves the highest degree of isotropy. According to Groth & Johansson (1988) several investigations have reported that the turbulence behind a grid retains a small degree of anisotropy over a very large downstream distance (up to $400M$).

The pressure gradient in the boundary layer was adjusted without a grid in the test section. The presence of the grids did not appear to affect the pressure gradient and figure 6 shows the pressure coefficient ($C_p$) plotted versus the downstream distance for three different injection rates of the active grid. As can be seen the mean flow condition is unchanged despite the different injection rates.

### 3.3.2. *Turbulence scales*

For the active grid the autocorrelation as well as the Taylor microscale were determined from a 60 s time series sampled at a frequency of 50 kHz. The integral scale was also determined from spanwise spatial correlation measurements using two hot wires. For the calculation of $\Lambda$ through (3.3) the integration limit was truncated at $t^* = 0.1$ s for the autocorrelation and $z^* = 70$ mm for the spatial correlation. In figure 7 the downstream evolution of $\tau$ and $\Lambda$ are plotted. It is clear that both scales increase with downstream distance. The integral length scale obtained from the spatial correlation (i.e. spanwise correlation of the streamwise velocity) is smaller than that obtained from the autocorrelation, which is in agreement with theoretical results for isotropic turbulence. The Taylor length scale increases with increasing injection, which is in agreement with the results in Gad-El-Hak & Corrsin (1974). A similar trend is apparent for the integral scale obtained from the spatial correlation measurements. For this free-stream velocity (5 m s$^{-1}$) the Taylor scale at the leading edge is in the interval 7–10 mm depending on the injection rate and the position of the grid.

### 3.3.3. *Energy spectra*

The energy spectra give a good overview of the turbulent scales for the different injection rates. If the energy distributions over the frequencies are the same it is likely that they also share the same energetic scales, i.e. turbulent length scales. When plotting the energy as $fE$ versus the frequency ($f$) for the no-injection case it is clearly seen that the main energy content moves towards lower frequencies with downstream distance, indicating an increase in size of the integral length scale (most energetic scale).

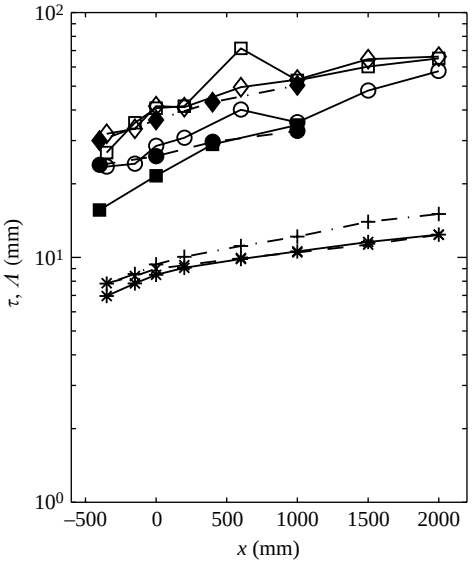


FIGURE 7. The Taylor ($\tau$) and integral ($\Lambda$) length scale evolution. □, *, G0; ○, ×, G1; ◇, +, G2. *, ×, + denotes $\tau$ and filled symbols are $\Lambda$ from spatial correlation measurements and unfilled symbols $\Lambda$ from the autocorrelation.

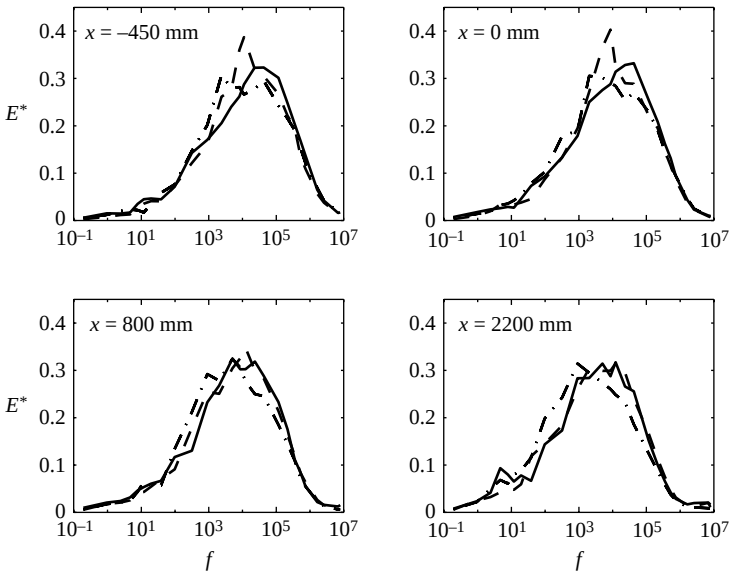


FIGURE 8. Energy spectra at different downstream positions for all three injection rates: G0 (solid), G1 (dashed), and G2 (dash-dotted). $E^* = fE/\int_0^\infty fE\,\mathrm{d}(\log f)$.

The energy spectra (normalized to make the total kinetic energy equal to unity) for all three injection rates are compared in figure 8 at different downstream positions. This figure shows that the variation of the energy distribution is small for the different injection rates, although a slight shift towards lower frequencies can be seen for increasing injection. It is also clearly seen that the maxima in the distributions move towards lower frequencies with downstream distance. A similar increase in the turbulence scales was observed in figure 7.

### 3.4. *Free-stream turbulence scales in the transition experiments*

In the previous sections we have described data for the different grids used in the present transition experiments. Each grid has been thoroughly evaluated at one free-stream velocity. According to (3.7) the Taylor scale for a given grid varies as $U_\infty^{-1/2}$ which for the present range of free-stream velocities (2–14 m s$^{-1}$) means a factor of 2.5 between the highest and lowest velocity. On the other hand the boundary layer thickness varies in the same way, so the ratio between the free-stream scales and the boundary layer thickness will not be affected by changing the free-stream velocity. What is also shown by (3.7) is that the Taylor scale increases with increasing distance from the grid. Each of the passive grids in the transition experiment was located at a specific $x$-position throughout the experiment, so in these cases there was no variation due to changes in position. The active grid on the other hand was moved to different positions upstream of the leading edge. This together with a variation with the injection rate gave rise to an almost 50% variation of the Taylor scale at the leading edge, which should be kept in mind when interpreting the transition results.

## 4. Intermittency estimation procedure

In an analysis of transitional flows, discrimination between turbulent and laminar flow is valuable not only to estimate the intermittency ($\gamma$) function but also to obtain separate statistics of the measured data for laminar and turbulent cases, i.e. conditional sampling. In order to do this there are two essential decisions that have to be made by the evaluator, i.e. choice of detector($\mathscr{D}$)/criterion ($\mathscr{C}$) function, and the determination of threshold value. The detector function is created from the velocity signal by some operation, e.g. first or second derivative or a high-pass filter, in order to sensitize the signal to increase its discriminatory capability. The criterion function is based on the detector function and is the function that is exposed to the selection (whether the signal is laminar or turbulent), which is based on the threshold value. So far there is no accepted universal procedure for the two decisions mentioned above. One difficulty is that the intermittency estimate is sensitive to the threshold value (typically an exponential dependence), which makes the choice of method essential and either more or less suitable for a given flow.

Hedley & Keffer (1974) discussed the difficulties in intermittency estimation and summarized many of the different $\mathscr{D}$-functions which had been used by different researchers. These ideas were further developed by Kuan & Wang (1990) who devised a general method to determine the threshold, the so-called 'dual-slope method'. In this method the second derivative of the velocity signal was adopted as the $\mathscr{D}$-function. The cumulative intermittency distribution as function of the threshold value appeared to consist of two straight lines of different slopes when plotted in a semilogarithmic diagram. The intersection of these lines was then chosen as the threshold value. With the data presented in this paper the change of slope was not always clear, making it difficult to determine the threshold in a clear cut manner. In our case the original idea in Hedley & Keffer (1974) of using the region of maximum curvature as threshold value may be more appropriate.

However, in the present work a slightly different approach is taken which also takes into account the downstream development of the fluctuations in the laminar parts of the signal. In figure 9 an example of the intermittency estimation is illustrated. Figure 9($a$) shows a velocity signal ($u$) with the absolute value of the corresponding high-pass filtered signal ($u_h$). The cut-off frequency ($f_{cut}$) for the filtering was chosen as $f_{cut} = U_\infty/(5\delta_{99})$, where $\delta_{99}$ is the Blasius-based boundary layer thickness. This

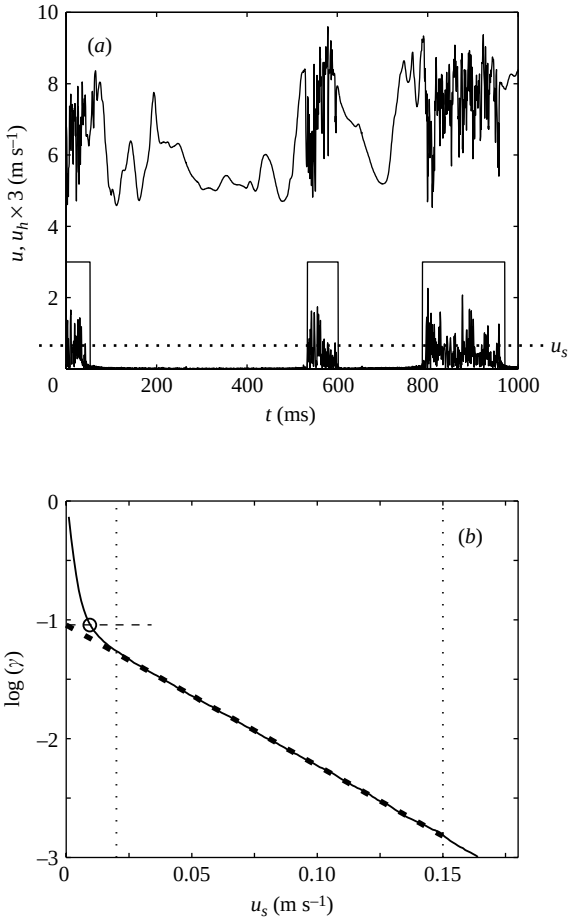


FIGURE 9. (*a*) Top velocity trace is the original signal ($u$) and the bottom trace is the corresponding high-pass filtered signal ($u_h$) (magnified by a factor of 3) with the intermittent regions marked with squares (i.e. the $\mathscr{I}_{u_s^*}$ function). $u_s$ is a threshold value. (*b*) Solid line corresponds to the intermittency of $u_h$ calculated by changing $u_s$, whereas the dashed line is the fitted line to obtain the intermittency at the intercept with the abscissa. The circle determines the value of $u_s^*$.

expression for $f_{cut}$ was selected through visual inspection of many different signals and is naturally based on the convective velocity ($\propto U_\infty$) and the streamwise scale ($\propto \delta_{99}$) of the streaky structures (cf. Matsubara & Alfredsson 2001). The $\mathscr{C}$-function is obtained by short-time averaging of the $\mathscr{D}$-function, in order to eliminate the zeros appearing in the turbulent regions. The threshold value ($u_s^*$) that will discriminate the true turbulence from the noise is determined by varying the level of $u_s$ in figure 9(*a*) on the $\mathscr{C}$-function, producing an indicator ($\mathscr{I}$) function according to

$$\mathscr{I}^j(t_i) = \begin{cases} 1 & \text{when} \quad \mathscr{C}(t_i) \geqslant u_s^j \\ 0 & \text{when} \quad \mathscr{C}(t_i) < u_s^j. \end{cases} \tag{4.1}$$

Here $i = 1 \ldots n$; and $j = 1 \ldots m$, where $n$ and $m$ are the number of discrete points of the signal and the number of threshold values, respectively. From the $\mathscr{I}$-function, $\gamma$ is calculated as function of $u_s$ which is plotted in figure 9(*b*) as a solid line. The

dashed line corresponds to

$$\gamma(u_s) = c\exp(\alpha u_s),$$

which is fitted to the calculated values between the dotted vertical lines. The intercept with the ordinate axis is used as the 'true' value of $\gamma$. The corresponding threshold value ($u_s^*$) giving the same $\gamma$ is marked in the figure by a circle.

## 5. Experimental data analyses

The presentation of the experimental results is divided into three sections. The first part deals with the streamwise disturbance energy growth. The streamwise disturbance energy level is shown to scale with $Re_x$ and the influence of the level of $Tu$ is discussed. The second part deals with quantitive results from the transition zone, obtained from intermittency measurements. The correlation between a transitional Reynolds number, based on the downstream distance from the leading edge, and the FST level is shown to agree according to the theoretical results by Andersson *et al.* (1999). Finally the present intermittency data are compared with two previously published models of the transition zone (Narasimha 1957; Johnson & Fashifar 1994). The universal intermittency functions according to these models are tested and parameters are proposed based on the present data. A new expression with a sound physical basis for the spot production rate, based on the present measurements, is also proposed.

### 5.1. *Disturbance energy growth*

In figure 10(*a*) the streamwise disturbance energy ($E = u_{\rm rms}^2/U_\infty^2$), measured at $y/\delta^* = 1.4$ ($\delta^* = 1.72\sqrt{xv/U_\infty}$ is the theoretical laminar displacement thickness of the Blasius boundary layer), is plotted as function of the Reynolds number (defined as $Re_x = xU_\infty/v$ throughout this paper). A typical curve shows an initial, nearly linear, growth after which the disturbance energy reaches a maximum and then asymptotes to a constant level around $E = 0.007$. By inspection it is found that the maximum is closely related to the point $\gamma = 0.5$, i.e. at this point the flow consists of alternating laminar portions and turbulent spots. The higher the $Tu$ the smaller the $Re_x$ for which the maximum occurs, i.e. transition occurs for smaller $Re_x$. Another feature of figure 10(*a*) is that the amplitude of the maximum increases with increasing $Tu$, or equivalently the maximum decreases the higher the associated $Re_x$.

There may be several reasons for the variation of the maximum value with $Re_x$. In the turbulent regions the $y$-position in terms of viscous units may change with $Re_x$ and thereby the difference in the mean velocity as compared with the laminar profile. A similar effect could change the turbulence intensity measured in the turbulent regions. Other possibilities include changes in streak spacing with $Tu$ which may change the growth or that transition occurs at lower streak amplitudes for higher $Re$. However in order to get a full understanding of this behaviour further experiments and analysis are required.

In figure 10(*b*) the measured points are plotted with the $x$-axis scaled with the interpolated $Re_x$-value for which $E = 0.01$ or equivalently $u_{\rm rms} = 0.1U_\infty$. As expected all points fall onto one curve; however the most interesting feature is that a line fitted through the points will cross the abscissa at some positive value of $Re_x$ (cf. the straight white/black line in figure 10*b*). This indicates that there is an initial region at the leading edge where the disturbances grow slower than further downstream. One possibility is that this is due to the receptivity process which needs a certain distance before it is completed and the disturbances have adjusted to the boundary layer.

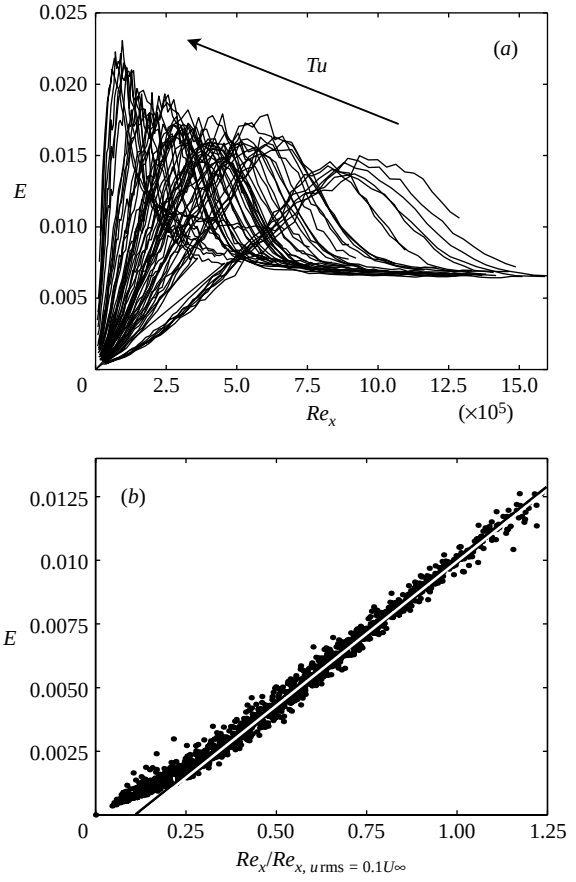


FIGURE 10. (*a*) Streamwise turbulent energy ($E = u_{\mathrm{rms}}^2/U_\infty^2$) as function of $Re_x$ for various free-stream turbulence levels. Measurements are made at $y/\delta^* = 1.4$. (*b*) Measured points in (*a*) where the horizontal axis is scaled with the position where $u_{\mathrm{rms}} = 0.1U_\infty$ (i.e. $E = 0.01$). The white/black straight line is fitted to the straight part of the data.

Figure 11 shows a measure of the disturbance growth ($\mathscr{G} = \mathrm{d}E/\mathrm{d}Re_x$), i.e. the slope of the linear region of a typical curve in figure 10(*a*). The slope is calculated by fitting a straight line in the interval of $E$ between 0.0025 and 0.0125. Here, the lower limit is determined by the above mentioned receptivity region where the disturbance evolution has a different slope, and the upper energy limit is where the intermittency starts to increase from zero (for $E < 0.0125$ $\gamma$ is always less than 0.1) and deviation from linear growth is to be expected. It can be seen that $\mathscr{G}$ is proportional to $Tu^2$. This result strongly indicates that there is a linear relation between the level of FST (forcing) and the disturbance amplitude (response) in the boundary layer. Note that the correlation between $\mathscr{G}$ and $Tu$ upon integration becomes

$$E \propto Tu^2 Re_x,$$

which is exactly the relation proposed by Andersson *et al.* (1999) based on transient growth theory together with the assumption of an initial energy quantity being proportional to the FST energy.

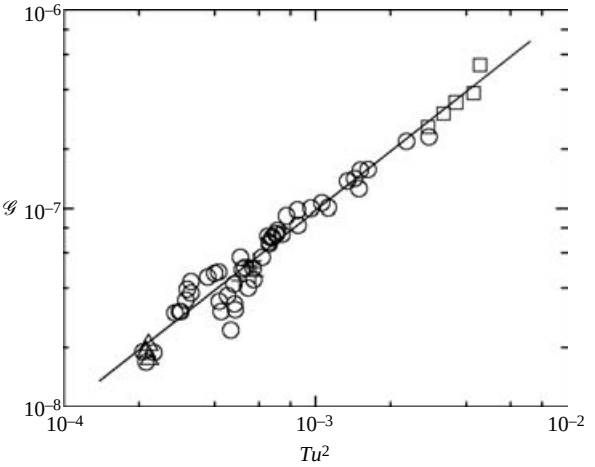


FIGURE 11. Slope of the linear growth in figure 10(*a*) versus $Tu^2$. The different symbols ($\triangle$, $+$, $\circ$, $\square$) correspond to the different turbulence generating grids (B, A, G, E), respectively.

### 5.2. *The transition zone*

In order to investigate the transition zone further the intermittency function for the different levels of $Tu$ was determined according to the procedure described in § 4. It is not obvious how to chose the best $y$-position to evaluate the intermittency. The following results were obtained by evaluating the intermittency at a position in the boundary layer where $y/\delta^* = 1.4$. However, as was shown in Matsubara, Alfredsson & Westin (1998) the intermittency is fairly constant up to at least $y/\delta^* = 2$.

Figure 12(*a*) shows the intermittency curves for seven different intensities of the FST: $Tu = 1.4\%$, 2.2%, 3.3%, 3.9%, 5.3%, 5.7%, 6.7%. They are shown as function of $Re_x/Re_{x,\gamma=0.5}$, i.e. they will all cross at the point [1, 0.5] in the plot. The figure shows that the relative length of the transition region increases with increasing turbulence level. Figure 12(*b*), on the other hand, shows that all the intermittency curves of the grid G cases that satisfy $Tu \leqslant 2.6\%$ collapse on a universal function.

The length of the transition zone is also an important variable for modelling as well as for a basic understanding of the transition process. In our experiments this length can be estimated from the intermittency function and we chose the values of $\gamma = 0.1$ and 0.9 to define the position where transition starts and ends, respectively. In the same way we define the middle of the transition zone as the position where $\gamma = 0.5$. In figure 13(*a*) the transition length is made non-dimensional in terms of a Reynolds number ($\Delta Re_{\rm tr} = Re_{x,\gamma=0.9} - Re_{x,\gamma=0.1}$) and plotted as function of the Reynolds number of the middle of the transition zone ($Re_{x,\gamma=0.5} = Re_{\rm tr}$), which we denote as the transitional Reynolds number. If we now estimate that the $x$-position where $\gamma = 0.5$ is the average value of those positions where $\gamma = 0.1$ and 0.9, we can introduce the shaded area in figure 13(*a*) which denotes non-admissible values of the transition-length Reynolds number. This relation states that $\Delta Re_{\rm tr} < 2Re_{\rm tr}$ and is arrived at from pure geometrical reasoning. The data from grids E and G appear to collapse on a single straight line whereas the data from grid A and grid B are above that line and thereby show a slightly longer transition zone. There may be several reasons for the differences between the grids, since the transition location is the result of a complex interaction of many processes: receptivity, algebraic growth as well as

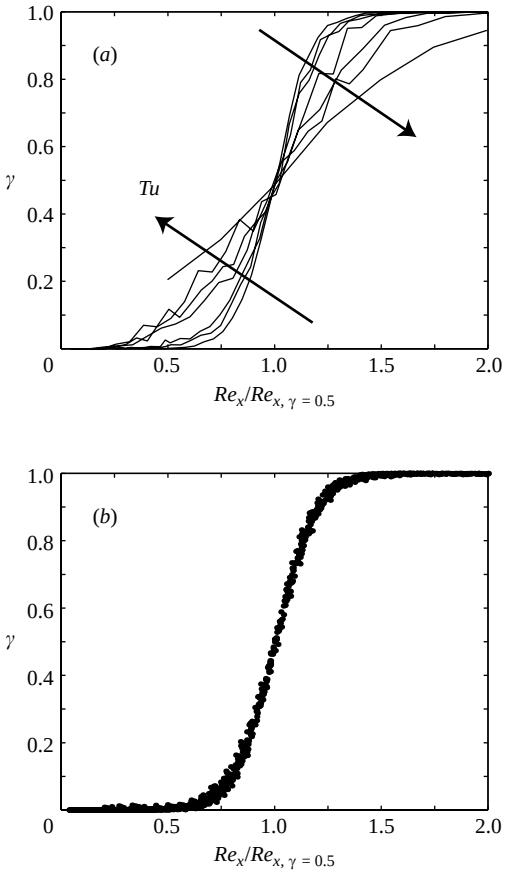


FIGURE 12. (*a*) Intermittency functions for different grids and *Tu* levels (1.4, 2.2, 3.3, 3.9, 5.3, 5.7, 6.7)%. (*b*) Intermittency functions from grid G and $Tu \leqslant 2.6\%$.

triggering and growth of secondary instability which all to some extent depend on the details of the FST. Note also that the line intercepts the vertical axis at a value of about $3.9 \times 10^4$, showing that there is a minimum length of the transition zone at high disturbance levels also. This is consistent with the idea of a minimum Reynolds number for self-sustained turbulence (see e.g Hall & Gibbings 1972).

The linear variation of $\Delta Re_{\rm tr}$ with $Re_{x,\gamma=0.5}$ can also be used to determine an expression for the relative length of the transition region. If we assume that there is a linear relation as in figure 13(*a*) this can be expressed as

$$\Delta Re_{\rm tr} = \Delta Re_{\rm tr,min} + kRe_{\rm tr} \tag{5.1}$$

where $\Delta Re_{\rm tr,min} = 3.9 \times 10^4$ is the intercept of the line with the ordinate axis and $k = 0.33$ is the slope. With this relation we can easily calculate the relative length of the start and end of transition such that

$$\frac{x_{0.9}}{x_{0.5}} = 1 + \frac{k}{2} + \frac{\Delta Re_{\rm tr,min}}{2Re_{\rm tr}} \tag{5.2}$$

and

$$\frac{x_{0.1}}{x_{0.5}} = 1 - \frac{k}{2} - \frac{\Delta Re_{\rm tr,min}}{2Re_{\rm tr}} \tag{5.3}$$

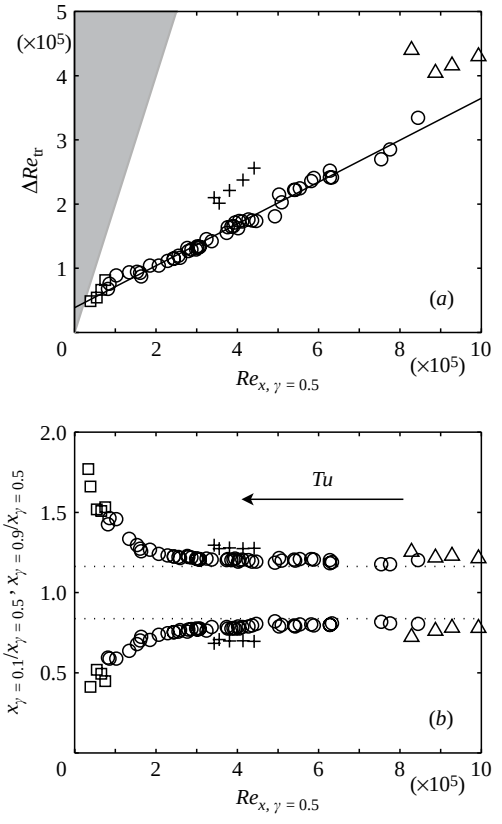


FIGURE 13. (*a*) Length of transition zone versus $Re_{x,\gamma=0.5}$. The shaded area denotes the non-admissable region for which $\Delta Re_{\mathrm{tr}} > 2Re_{x,\mathrm{tr}}$. (*b*) Downstream position where $\gamma = 0.1$ (lower set of symbols) and 0.9 (upper set) normalized with the position where $\gamma = 0.5$. The dotted lines correspond to $1 \pm \frac{1}{2}k$ where $k = 0.33$ (see equations (5.2) and (5.3)). See caption of figure 11 for symbols.

As can be seen, the relative length tends to a constant value for large transition Reynolds numbers whereas it becomes larger for small $Re_{\mathrm{tr}}$. This is illustrated in figure 13(*b*) where the individual values are plotted. The assumption that the position of $\gamma = 0.5$ is in the middle between the values of $\gamma = 0.1$ and 0.9 seems to be fairly accurate.

There have been other attempts to relate the length of the transition zone to the transition Reynolds number. For instance Dhawan & Narasimha (1957) and later Narasimha (1984) suggested a power-law relation such that

$$\Delta Re_{\mathrm{tr}} = \alpha Re_{\mathrm{tr}}^{\beta}. \tag{5.4}$$

The values of $\alpha$ and $\beta$ given in Narasimha (1984) were 9.0 and 0.75, respectively, where they used the levels of $\gamma = 0.25$ and 0.75 to determine the length of the transition zone. However according to equation (5.1) there is a minimum length of the transition zone and therefore (5.4) must diverge from the experimental data for small values of $Re_{\mathrm{tr}}$, i.e. high levels of $Tu$. In figure 14 the same data as in figure 13 are plotted, but now in logarithmic format and with $(\Delta Re_{\mathrm{tr}} - \Delta Re_{\mathrm{tr,min}})$ as function of $Re_{\mathrm{tr}}$, where $\Delta Re_{\mathrm{tr,min}} = 3.9 \times 10^4$. We also plot the data from grid G (shown as dots),

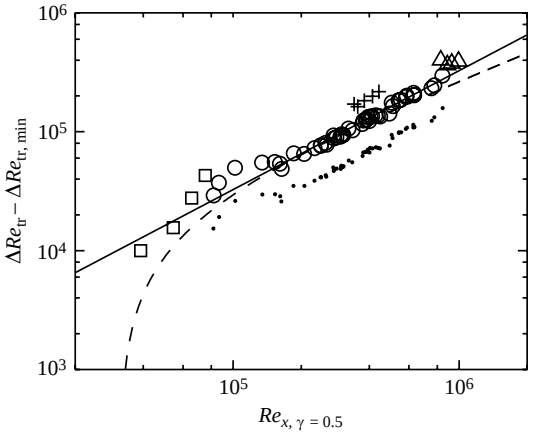


FIGURE 14. Correlation between the length of transition zone and the Reynolds number at the end of transition. The symbols (△, +, ○, □) correspond to the different turbulence generating grids (B, A, G, E) using $\gamma = 0.1$ and 0.9 to determine the length of the transition zone, whereas the bold dots correspond to the same case as ○ but where the transition length was determined using $\gamma = 0.25$ and 0.75. $\Delta Re_{tr,min}$ for the two cases is $3.9 \times 10^4$ and $2.1 \times 10^4$, respectively. ——, The best fit to the ○; – – –, the function suggested by Narasimha (1984). Note that this line should fit the data obtained using $\gamma = 0.25$ and 0.75.

using the shorter transition zone (i.e. $0.25 < \gamma < 0.75$) from Narasimha (1984). In that case a different $\Delta Re_{tr,min}$ ($= 2.1 \times 10^4$), belonging to the corresponding definition of the transition zone length, has been used. Also plotted in the figure are the two expressions (5.1) and (5.4). First of all it is clear that the present data follow expression (5.1). Equation (5.4) with the values suggested by Narasimha (1984) should follow the data obtained with $0.25 < \gamma < 0.75$; however the length of the transition zone is over-predicted by nearly a factor of two. For small values of $Re_{tr}$ or high values of $Tu$ the Narasimha (1984) curve becomes unphysical as expected.

The intermittency data can also be used to estimate the transition Reynolds number $Re_{tr}$, which we define to be the Reynolds number for which $\gamma = 0.5$. Figure 15 shows the transitional Reynolds number as function of $Tu$ for all four grids. In both plots the line corresponding to

$$Re_{x,\gamma=0.5} = C\,Tu^{-2} \tag{5.5}$$

is also shown, which is seen to give a good representation of the data. This is in agreement with the suggestion by Andersson *et al.* (1999) that for FST-induced transition the breakdown to turbulence occurs when the streaky disturbances in the boundary layer reach a certain (high) amplitude (This assumption is, however, not fully supported by the results in figure 10(*a*)). They also assumed that the input energy is proportional to the FST energy and that the streaky structures grow in amplitude with the optimal rate. These assumptions lead to $Re_{tr}$ being proportional to $Tu^{-2}$. In that paper this idea was substantiated by comparisons with experimental data by Matsubara, Yang & Voke, and Roach & Brierley, as well as with the semiempirical correlation curve by van Driest & Blumer (for detailed references see Andersson *et al.* 1999). The present data give $C = 196$, compared to $C = 144$ suggested in Andersson *et al.* However, there are several factors that influence the $C$-value, such as the definition of the transitional Reynolds number, the degree of anisotropy, the leading-edge suction peaks, the small deviation from a zero pressure gradient throughout the

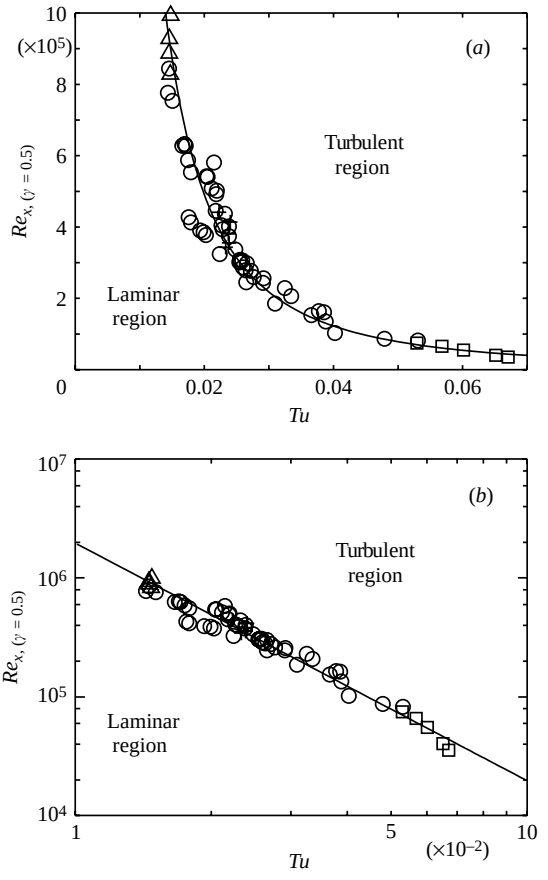


FIGURE 15. (*a*) Transitional Reynolds number (defined from $\gamma = 0.5$) as function of the free-stream turbulence level. (*b*) Logarithmic axes of the data in (*a*). See caption of figure 11 for symbols. Solid line is a curve fit to the symbols according to equation (5.5).

test section, scales and energy spectrum of the free-stream turbulence etc. It should be mentioned that with the transitional Reynolds number defined where $\gamma = 0.1$, we obtain a $C$-value of about 126, i.e. below the value proposed by Andersson *et al.*

### 5.3. *Intermittency models*

Emmons (1951) formulated a theory which describes the relation between a spot production function $[g(x, z, t)]$ and the intermittency factor $[\gamma(x)]$, based on probability considerations. For a steady two-dimensional flow this relation is

$$\gamma(x) = 1 - \exp\left[-\int_{\mathscr{R}} g(x_0)\,\mathrm{d}x_0\,\mathrm{d}z_0\,\mathrm{d}t_0\right], \tag{5.6}$$

where $\mathscr{R}$ is the dependence volume (spot sweep volume) assumed to be a cone with straight generators. However, due to the lack of available experimental data Emmons suggested a simple assumption about $g(x)$, namely that it be independent of $x$. Six years later Narasimha (1957) improved this assumption based on new observations. These observations suggested that laminar breakdown in a two-dimensional boundary layer is nearly point-like, and that the spots originate in a restricted region (see

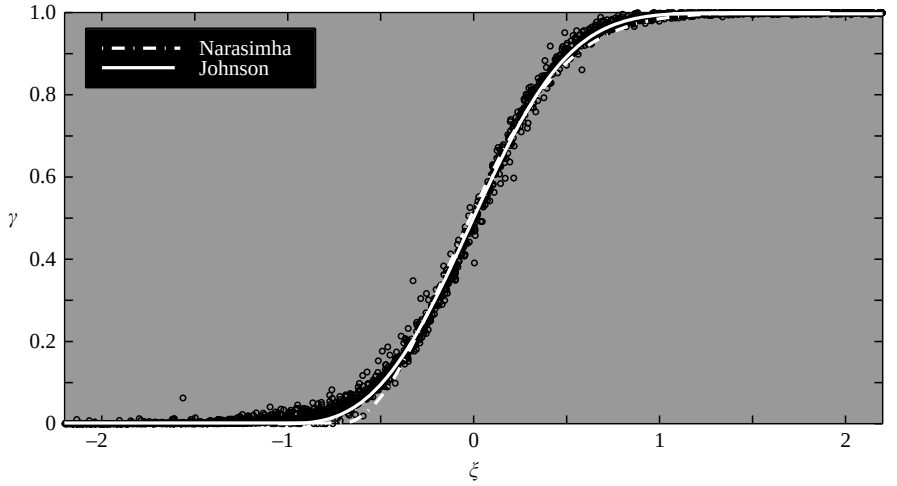


FIGURE 16. Universal intermittency functions corresponding to equations (5.8) (Narasimha model) and (5.9) (Johnson model) compared with all the experimental data shown as circles.

Dhawan & Narasimha 1957 for an extended version of Narasimha 1957). Dhawan & Narasimha (1957) argue that $g(x)$ should have a maximum at some location and they state that experimentally this location turns out to be the position of the start transition ($x_t$). Assuming a Gaussian distribution to represent $g(x)$ with its centre at $x_t$, they showed that the best fit of the Gaussian curve to experimental data is achieved when the standard deviation approaches zero (i.e. nearly a Dirac delta function, $\delta(x)$). Applying $g(x_0) = n\delta(x_0 - x_t)$ in (5.6) Narasimha (1957) derived the following expression:

$$\gamma(x) = 1 - \exp\left[-(x - x_t)^2 \frac{n\sigma}{U_\infty}\right], \tag{5.7}$$

where $n\sigma/U_\infty$ is assumed constant with $n$ and $\sigma$ being the turbulent spot production rate per unit length in the spanwise direction and Emmon's dimensionless spot propagation parameter, respectively. Furthermore, he showed that $\gamma$ can be expressed as a unique function of $\xi$ according to

$$\gamma(x) = 1 - \exp[-A_N(\xi + B_N)^2], \tag{5.8}$$

where $\xi = (Re_x - Re_{tr})/\Delta Re_{tr}$, and $A_N$ and $B_N$ are constants.

Johnson & Fashifar (1994) used a different approach resulting in an ordinary differential equation for $\gamma$. Furthermore, they assumed $n\sigma/U_\infty$ to increase linearly with $x$ resulting in a unique function for $\gamma$ like (5.8) but with the exponent $\xi$ appearing as a power of 3 (instead of 2) according to

$$\gamma(x) = 1 - \exp[-A_J(\xi + B_J)^3], \tag{5.9}$$

where $A_J$ and $B_J$ are constants.

In figure 16 all $\gamma$-distributions corresponding to different $Tu$-levels are plotted and they all show a common distribution. In the same figure both the Narasimha and the Johnson $\gamma$-functions are shown as dashed and solid lines, respectively. The best fit to all data results in $(A_N, B_N) = (1.42, 0.72)$ and $(A_J, B_J) = (0.60, 1.05)$, respectively,

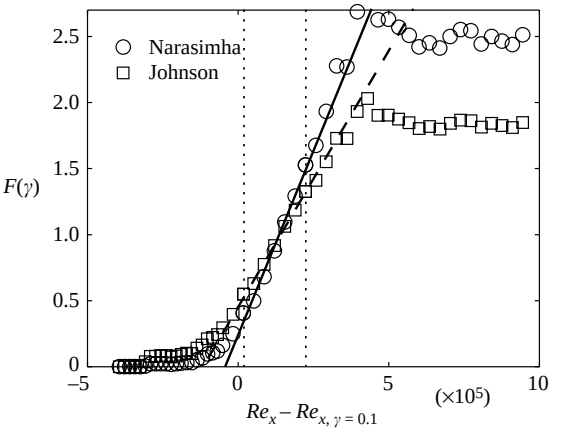


FIGURE 17. Procedure for determination of $Re_{\mathrm{tr,start}}$. Same data is applied for the Narasimha and the Johnson models.

where the Johnson model is seen to give the best representation. It can be noted that an exponent slightly larger than 3 would give an even better fit to the data.

Finally, by introducing $Re_x$ in (5.7) the Narasimha model may be transformed to

$$\gamma(x) = 1 - \exp[-(Re_x - Re_{x,\mathrm{t}})^2 \hat{n}\sigma], \tag{5.10}$$

where $\hat{n} = nv^2/U_\infty^3$ is a dimensionless spot production parameter. Note that comparison with (5.8) reveals the relation $\hat{n}\sigma \propto \Delta Re_{\mathrm{tr}}^{-2}$.

An interesting correlation in this context is the one between the position where transition starts ($Re_{\mathrm{tr,start}}$) and the *Tu*-level. For this, one has to define the start of transition. Mayle (1991) (see his Appendix B) outlines a method to determine this position based on the function

$$F(\gamma) = [-\log(1-\gamma)]^{1/p}$$

suggested in Narasimha (1957) (where $p = 2$). Through straight-line curve fitting in the range $0.1 < \gamma < 0.9$, $Re_{x,\mathrm{t}}$ (in (5.10)) is determined by the $Re_x$ value where the line crosses the ordinate (i.e. $F(\gamma) = 0$). An example is shown in figure 17 where $F(\gamma)$ for both the Narasimha ($p = 2$) and the Johnson ($p = 3$) models are plotted.

This procedure is repeated for all cases (and both models) and in figure 18 $Re_{\mathrm{tr,start}}$ is plotted versus the *Tu*-level together with the $Re_x$ where $\gamma = 0.1$ (+symbols). A best fit to the +symbols according to $Re_{\mathrm{tr,start}} = K\,Tu^m$ with $m = -2$ is calculated, resulting in $K = 126$, and compared with the model by Mayle corresponding to $(K, m) = (1148, -5/4)$. From the figure we can conclude that $Re_{x,\gamma=0.1}$ corresponds well with the Narasimha model and that the Johnson model defines the start of transition to be slightly earlier (i.e. for a lower $\gamma$-value). For high *Tu* the Johnson model even produced some values of the start of transition that were located upstream of the leading edge of the plate. These are of course excluded from figure 18.

From (5.10) it is clear that the slope of the curve corresponds to $\sqrt{\hat{n}\sigma}$, which is related to the transition length as stated above. In figures 19(*a*) and 19(*b*) the non-dimensional spot production rate ($\hat{n}\sigma$, obtained from the Narasimha model) is plotted versus $\Delta Re_{\mathrm{tr}}$ and *Tu*, respectively. Figure 19(*a*) simply verifies the proportionality stated above and the solid line in the figure corresponds to $\hat{n}\sigma = 1.52\Delta Re_{\mathrm{tr}}^{-2}$. With this result, together with (5.5) and (5.1), it is possible to write down an expression for

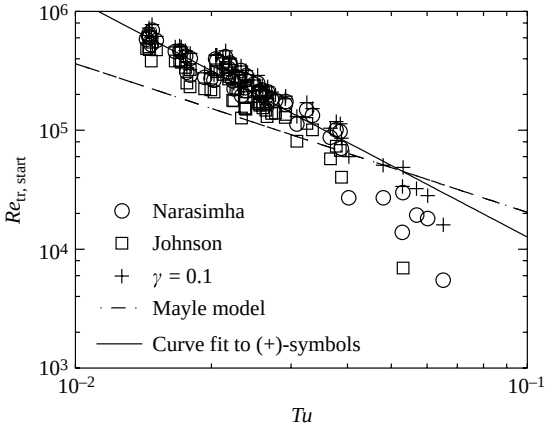


FIGURE 18. Start position of transition zone versus $Tu$ (see text for comments).

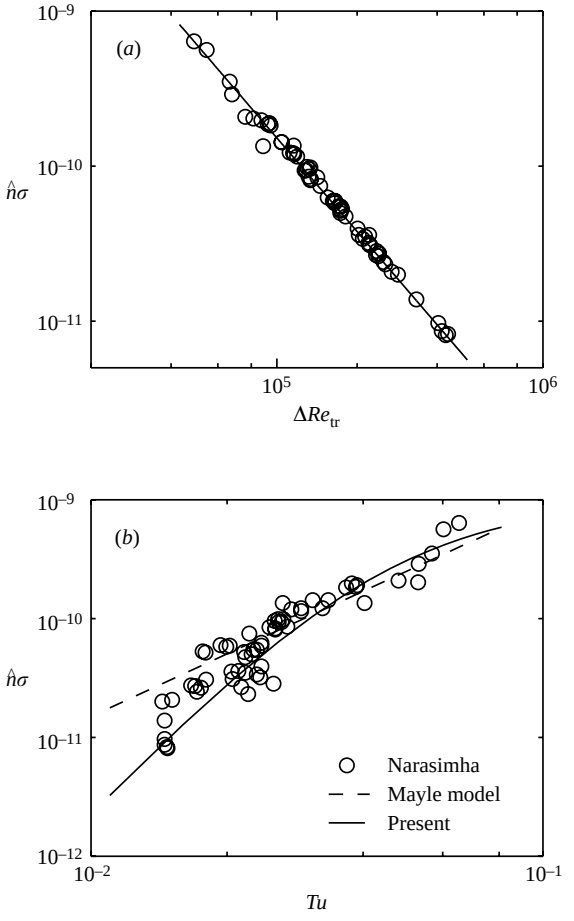


FIGURE 19. Non-dimensional spot production rate versus (*a*) the extent of the transition zone solid line is $\hat{n}\sigma = 1.52\Delta Re_{tr}^{-2}$; and (*b*) turbulence intensity level, solid line is $\hat{n}\sigma = 10^{-9}(1 + 0.00165Tu^{-2})^{-2}$.

the variation of $\hat{n}\sigma$ with $Tu$ such that

$$\hat{n}\sigma = \frac{1.52}{\Delta Re_{\mathrm{tr,min}}^2}\left(1 + \frac{kC}{\Delta Re_{\mathrm{tr,min}}} Tu^{-2}\right)^{-2} \tag{5.11}$$

where the values of the constants have been given earlier but are repeated here: $k = 0.33$, $C = 196$ and $\Delta Re_{\mathrm{tr,min}} = 3.9 \times 10^4$. In figure 19($b$) we compare the Mayle (1991) model ($\hat{n}\sigma = 4.7 \times 10^{-8} Tu^{7/4}$) with the present data. Also included in the figure is the curve obtained from (5.11). It is seen that this expression follows the data better than the Mayle model, and, especially, seems to give the correct behaviour for low $Tu$, where (5.11) shows $\hat{n}\sigma$ to become proportional to $Tu^4$. For levels of $Tu$ less than 0.5%–1%, TS-waves start to dominate the transition process and then (5.11) ceases to be valid. On the other hand, high values of $Tu$ give a constant value of $\hat{n}\sigma$. This can be seen as a result of a minimum Reynolds number for transition, i.e. for high $Tu$ a further increase does not lower $Re_{\mathrm{tr}}$ and hence $\hat{n}\sigma$ appears to stay constant.

## 6. Summary and conclusions

This paper describes an extensive set of measurements of free-stream-turbulence-induced transition for turbulence levels ranging from 1.4% to 6.7% of the free-stream velocity. The following points summarize the results:

(i) A procedure to estimate the intermittency of a velocity signal has been developed and implemented successfully to determine flow properties in the transitional zone.

(ii) There is an initial region at the leading edge where the disturbances grow more slowly than further downstream, which is hypothesized to be connected to the receptivity process where the FST scales need some distance to adjust to the boundary layer.

(iii) In the initially laminar but disturbed region, it has been found that the disturbance energy ($E = u_{\mathrm{rms}}^2/U_\infty^2$) is proportional to $Tu^2 Re_x$. This verifies the theoretical results of Andersson *et al.* (1999) and Luchini (2000) that disturbances should grow as $Re_x$ as well as the hypothesis by Andersson *et al.* (1999) that there is a linear response of the boundary layer to the disturbance energy of the FST.

(iv) The transitional Reynolds number was found to vary as $Tu^{-2}$.

(v) It was found that the non-dimensional length of the transitional zone has a minimum value and it increases linearly with $Re_{\mathrm{tr}}$. This result casts doubt on earlier attempts to model the length of the transitional zone.

(vi) For $Tu \gtrsim 2.5\%$ the relative length of the transitional zone increases with increasing $Tu$.

(vii) The intermittency function is found to have a relatively well-defined distribution, valid for all $Tu$.

We may also conclude that the present results seem to confirm that the initial part of the transition scenario is due to algebraically growing disturbances and that the prediction method of Andersson *et al.* (1999) rests on a sound physical basis.

Finally we were able to relate $Re_{\mathrm{tr}}$ and $Tu$ to the spot production rate in a way which gives a better physical description of the transitional zone than has previously been obtained.

This research is partly financed through VR, The Swedish Research Council. M. M. was supported by JSPS Research Fellowships for Young Scientists. Dr Johan Westin took part during earlier phases of this research and was also very helpful in locating

some missing data. Professor D. S. Henningson and Dr L. Brandt are acknowledged for useful discussions and Dr J. Shiomi for taking part in the construction work of the active grid and for some of the initial data collection.

## REFERENCES

Andersson, P., Berggren, M. & Henningson, D. S. 1999 Optimal disturbances and bypass transition in boundary layers. *Phys. Fluids* **11**, 134–150.

Brandt, L., Schlatter, P. & Henningson, D. S. 2004 Transition in boundary layers subject to free-stream turbulence. *J. Fluid Mech.* **517**, 167–198.

Dhawan, S. & Narasimha, R. 1957 Some properties of boundary layer flow during the transition from laminar to turbulent motion. *J. Fluid Mech.* **3**, 418–436.

Emmons, H. W. 1951 The laminar-turbulent transition in a boundary layer–Part I. *J. Aero. Sci.* **18**, 490–498.

Fransson, J. H. M. 2004 Leading edge design process using a commercial flow solver. *Exps. Fluids* **37**, 929–932.

Fransson, J. H. M. & Alfredsson, P. H. 2003 On the disturbance growth in an asymptotic suction boundary layer. *J. Fluid Mech.* **482**, 51–90.

Fransson, J. H. M., Brandt, L., Talamelli, A. & Cossu, C. 2004 Experimental and theoretical investigation of the nonmodal growth of steady streaks in a flat plate boundary layer. *Phys. Fluids* **16**, 3627–3638.

Gad-El-Hak, M. & Corrsin, S. 1974 Measurements of the nearly isotropic turbulence behind a uniform jet grid. *J. Fluid Mech.* **62**, 115–143.

Groth, J. & Johansson, A. V. 1988 Turbulence reduction by screens. *J. Fluid Mech.* **197**, 139–155.

Hall, D. J. & Gibbings, J. C. 1972 Influence of stream turbulence and pressure gradient upon boundary layer transition. *J. Mech. Engng Sci.* **14**, 134–146.

Hallbäck, M., Groth, J. & Johansson, A. V. 1989 A Reynolds stress closure for the dissipation in anisotropic turbulent flows. *Seventh Symposium on Turbulent Shear Flows, Stanford University*, vol. 2, pp. 17.2.1–17.2.6.

Hedley, T. B. & Keffer, J. F. 1974 Turbulent/non-turbulent decisions in an intermittent flow. *J. Fluid Mech.* **64**, 625–644.

Jacobs, R. G. & Durbin, P. A. 2001 Simulations of bypass transition. *J. Fluid Mech.* **428**, 185–212.

Johansson, A. V. & Alfredsson, P. H. 1982 On the structure of turbulent channel flow. *J. Fluid Mech.* **122**, 295–314.

Johnson, M. W. & Fashifar, A. 1994 Statistical properties of turbulent bursts in transitional boundary layers. *Intl J. Heat Fluid Flow* **15**, 283–290.

Kendall, J. M. 1985 Experimental study of disturbances produced in a pre-transitional laminar boundary layer by weak free-stream turbulence. *AIAA Paper* 85–1695.

Kendall, J. M. 1998 Experiments on boundary-layer receptivity to free-stream turbulence. *AIAA Paper* 98-0530.

Klingmann, R. G. B., Boiko, A. V., Westin, K. J. A., Kozlov, V. V. & Alfredsson, P. H. 1993 Experiments on the stability of Tollmien-Schlichting waves. *Eur. J. Mech.* B/*Fluids* **12**, 493–514.

Kuan, C. L. & Wang, T. 1990 Investigation of the intermittent behaviour of transitional boundary layer using a conditional averaging technique. *Expl Therml Fluid Sci.* **3**, 157–173.

Lindgren, B. 2002 Flow facility design and experimental studies of wall-bounded turbulent shear flows. PhD thesis, KTH, Stockholm, *TRITA-MEK Tech. Rep.* 2002:16.

Luchini, P. 2000 Reynolds-number independent instability of the boundary layer over a flat surface. Part 2. Optimal perturbations. *J. Fluid Mech.* **404**, 289–309.

Matsubara, M. & Alfredsson, P. H. 2001 Disturbance growth in boundary layers subjected to free-stream turbulence. *J. Fluid Mech.* **430**, 149–168.

Matsubara, M., Alfredsson, P. H. & Westin, K. J. A. 1998 Boundary layer transition at high levels of free-stream turbulence. *ASME paper* 98-GT-248.

Mayle, R. E. 1991 The role of laminar-turbulent transition in gas turbine engines. *J. Turbomach.* **113**, 509–537.

Narasimha, R. 1957 On the distribution of intermittency in the transition region of a boundary layer. *J. Aero. Sci.* **24**, 711–712.

Narasimha, R. 1984 Subtransitions in the transition zone. In *Proc. IUTAM Symposium, Laminar–Turbulent Transition* (ed. V. Kozlov), pp. 141–151. Novosibirsk: Springer.

Oberlack, M. 2002 On the decay exponent of isotropic turbulence. In *PAMM–Proc. Appl. Math. Mech.*, vol. 1, pp. 294–297. Weinheim, Germany: Wiley-VCH Verlag GmbH.

Tennekes, H. & Lumley, J. L. 1997 *A First Course in Turbulence*. The MIT Press.

Westin, J. 1997 Laminar-turbulent boundary layer transition influenced by free-stream turbulence. PhD thesis, KTH, Stockholm, *TRITA-MEK Tech. Rep.* 1997:10.

Westin, K. J. A., Boiko, A. V., B. G. B. Klingmann, V. V. K. & Alfredsson, P. H. 1994 Experiments in a boundary layer subjected to free-stream turbulence. Part I. Boundary layer structure and receptivity. *J. Fluid Mech.* **281**, 193–218.

Yoshioka, S., Fransson, J. H. M. & Alfredsson, P. H. 2004 Free-stream turbulence induced disturbances in boundary layers with wall suction. *Phys. Fluids* **16**, 3530–3539.